

Liquid Chain Genesis by Collision of Two Laminar Jets

Vatsal Sanjay^{1, a)} and Arup Kumar Das^{1, b)}

*Department of Mechanical and Industrial Engineering, Indian Institute of Technology,
Roorkee*

(Dated: 3 June 2017)

Liquid chain genesis is studied through a series of fully resolved numerical simulations. The transient process of collision of liquid jets and subsequent formation of a sheet in the median plane, perpendicular to the axes of impinging jets is illustrated and analyzed to pertain towards a steady state in which a chain like fluidics structure is formed, with subsequent sheets forming the respective links of the chain in mutually orthogonal planes. Flow kinematics is studied with self-similar velocity profile in the sheet varying with the azimuthal angle. Further, streamlines of the flow are analyzed at length to understand the behavior of fluid parcels inside the sheet and at the location of subsequent collisions. A wide range of parametric variations is tackled to understand the effects of physical and kinematic properties on the chain structure. Further, two different models using regression and analogy of billiard balls collision, are proposed to predict the shape and size of the primary link. On one hand, the former gives information about the dimensions of the link to a better accuracy, the latter force balance model using the billiard balls analogy gives an insight into the Physics of the problem. At last, special attention is given to the second and third collisions that form liquid sheets orthogonal to the preceding link and the mode of collision can be generalized for the entire chain structure.

Keywords: Impinging jets, Liquid sheet, Fluid chain

^{a)}Electronic mail: vatsalsanjay@gmail.com

^{b)}Electronic mail: arupdas80@gmail.com

I. INTRODUCTION

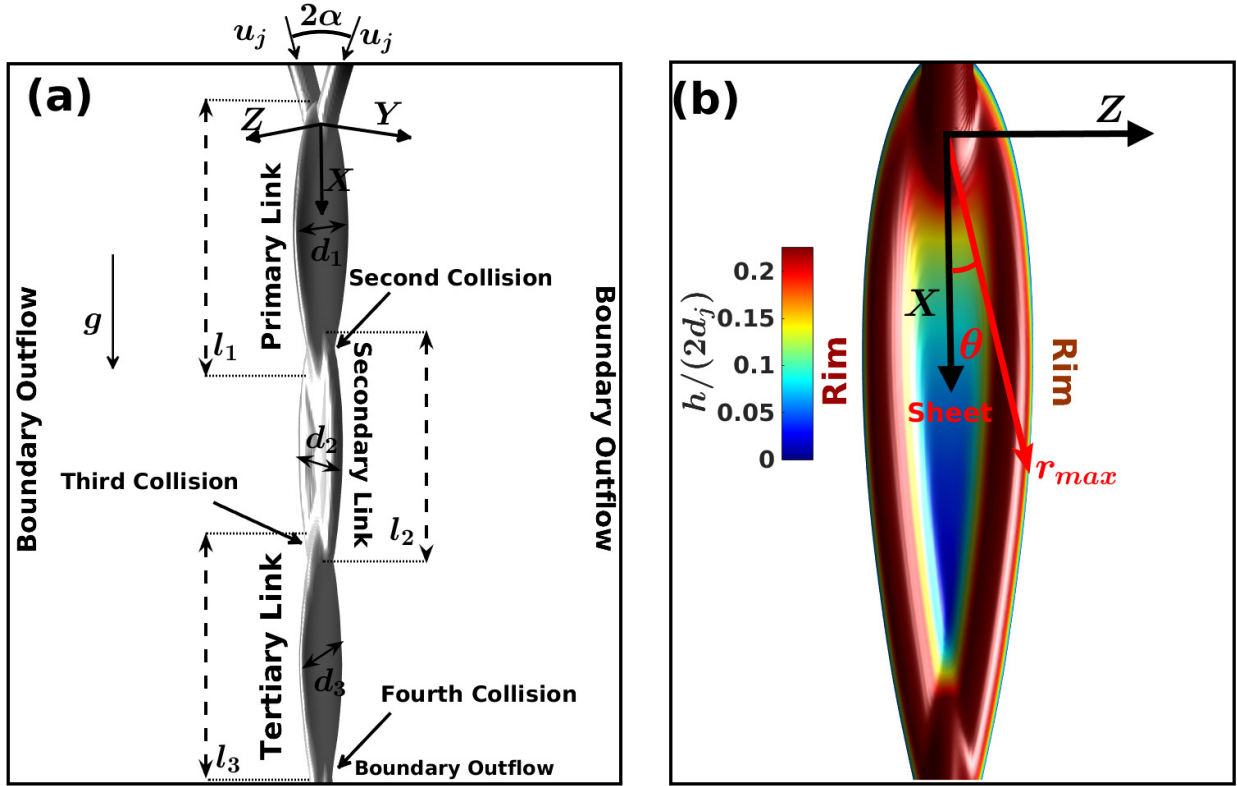


FIG. 1. Formation of the liquid sheet by collision of laminar jets. (a) A schematic to illustrate different structural features and length scales. The mutually perpendicular sheets mark different links of the fluid chain structure. (b) The primary link structure colored based on half times the magnitude of the sheet thickness, non-dimensionalized with the jet diameter ($\frac{h}{2d_j}$).

Interactions of liquid jets have invoked the curiosity of researchers with their ubiquitous presence (Eggers and Villermaux, 2008) ever since the 16th century, eminent in the works of Leonardo Da Vinci as reported by Da Vinci, Schneider, and Gingerich (1999). One of these interactions is the collision of liquid jets presented by Rayleigh (1879) and the references therein. Collision of impinging jets result in formation of a liquid sheet perpendicular to the plane of the jets. Bush and Hasha (2004) introduced several regimes to characterize the different flow structures obtained from such collisions, working on the theory of liquid jet impingement given by Taylor (1960). At low velocities or small angles of impingement (near to vertical jets), the two jets may coalesce to form a single jet or bounce off due to presence of a thin film of air between them (Wadhwa, Vlachos, and Jung, 2013). The

recoil of such jets is surface tension dominated. On increasing the flow rates, laminar jets may lead to formation of a stable liquid sheet bounded by a thick rim (Yang *et al.*, 2014). Inertia and body forces (gravity) act to expand the liquid sheet formed but the action of surface tension force puts a check on this expansion and the sheet converges, such that the successive collisions of the thick rims downstream of the flow result in formation of mutually orthogonal liquid sheets (Bush and Hasha, 2004). Figure 1a illustrates this structure which has been termed as the liquid chain with the complementary orthogonal sheets forming the different links. As the velocity of the jets is increased, Kelvin - Helmholtz type of instability takes control (Bremond and Villermaux, 2006), resulting in the formation of destabilizing waves (Villermaux and Clanet, 2002) which leads to ejection of droplets from the liquid rim featuring Plateau-Rayleigh instability through mechanisms explained by Lhuissier and Villermaux (2011). Further increase in velocities marks the transition of the regime from fluid fishbones into vigorously flapping sheet leading to atomization (Ibrahim and Przekwas, 1991). This process has been employed as an efficient method of fuel injection system in liquid propellant rocket engines because of its high mixing efficiencies. Unsurprisingly, most of the works on collision of liquid jets revolve around the regime of atomization (Miller Jr, 1960; Ibrahim and Przekwas, 1991; Bremond and Villermaux, 2006; Chen *et al.*, 2013; Zheng *et al.*, 2015). However, the presence of droplets make the study that of multi-scale and requires huge computational resources. The stable close rim chain regime is not just an idealization of the more violent flapping regime, but also holds physical significance for the exploration of fundamental Physics of the process. Moreover, these structures can be used as wall-free continuous reactors (Erni and Elabbadi, 2013) and are often used as a canonical arrangement for generation of liquid sheets (Dombrowski and Fraser, 1954). Therefore, we delve into the formation of stable closed liquid sheets and the consequent chain structure (Figure 1).

A wide range of experimental works can also be found which explores the formation of stable liquid sheets using viscous jets. Emphasis has been given on predicting the shapes of the leaf-like links formed in the chain structure and results of model by Bush and Hasha (2004) give a remarkable correspondence with the experimental observations. However, the model requires input from the experiments in order to close the system of differential equations. The results from their work have been used to validate our mathematical model in Section III. The formation of these links in the chain structure is extremely sensitive to

the initial velocity profile of the liquid jet at the entry of domain as argued by Choo and Kang (2002, 2007); Inamura and Shirota (2014). Experiments show that the jet velocity near the inlet plane follows a parabolic profile (Choo and Kang, 2002). Incorporation of this velocity profiles for laminar jets can refine the results obtained with the numerical simulations (Chen *et al.*, 2013). Therefore, a fully developed parabolic velocity profile has been adapted for the laminar liquid jet at inlet as discussed in the Section II. Further, using Particle Image Velocimetry (PIV) technique, radial streamlines are observed near the point of impingement and the fluid parcels travel towards the periphery resulting in the formation of the thick rim because of fluid accumulation (Choo and Kang, 2002; Bush and Hasha, 2004). The rim is stable as long as the curvature force developed by surface tension provides the necessary centripetal acceleration as the fluid packets in the rim accelerate owing to loss in gravitational potential (Bremond and Villermaux, 2006). On balancing the two, Taylor (1960) developed an expression for the sheet radius, given by $r_{max} = \rho u_0 Q(\theta)/(2\sigma)$ (where, u_0 denotes the average sheet velocity, $Q(\theta)$ implies the liquid flux distribution within the sheet and ρ and σ are the fluid density and surface tension coefficient with air respectively) and has been found to describe the experimental results of Bush and Hasha (2004). However, in most of the numerical work done so far, the velocity of the liquid sheet has been assumed to be constant and effect of forces because of viscosity of the fluid and drag offered by surrounding air medium are neglected (Taylor, 1960; Hureau and Weber, 1998; Bush and Hasha, 2004).

It is necessary to investigate the phenomenon with a fully resolved closed form solution of the Navier-Stokes equations in a three dimensional framework. Chen *et al.* (2013); Ma *et al.* (2011) used an improved Volume of Fluid technique with Adaptive Mesh Refinement (AMR) coupled with the Finite Volume Method to delve into the different regimes of flow structures formed on collision of liquid jets, from the stable chain structure to violent flapping liquid sheet atomization. We use the same mathematical model with efforts to concentrate on the fluid chain regime with attempts to understand the flow inside the sheet and characteristics of the primary link. Special attention is also provided to the mechanism of formation of the secondary links of chain structure, which can be extended to the tertiary links as well. Chen *et al.* (2013) validated the numerical model with the results from the theoretical works of Bremond and Villermaux (2006), and we have carried out a similar validation with the experimental results of Bush and Hasha (2004). Apart from Chen *et al.* (2013), there have

been only a few other works for the numerical simulation of the process, because of the complexity that arises due to multiple length scales (from the jet diameters (d_j) to liquid sheet thickness ($\sim 10^{-2}d_j$), the sheet has minimum thickness just upstream of the second collision as shown in Figure 1b. Inoue, Watanabe, and Himeno (2008, 2009) attempted to simulate the atomization regime of liquid jets collision with less than 50 grid points across the diameter of the jets, leading to inability in tracking of the small scale droplets and sheet thickness way downstream of the point of collision. Other works include the simulations by Arienti *et al.* (2012) which is also in the atomization regime, whereby the combined level-set and volume of fluid technique (Sussman *et al.*, 2007) was used coupled with Lagrangian Point Particle (LPP) tracking for the small scaled droplets. Recently, Da *et al.* (2016) developed an innovative technique for simulations using surface only fluids, whereby only surface velocity fields are solved using the Boundary Element Method (BEM) on a three dimensional framework, but suffers from the same inviscid assumption taken in earlier theoretical works. Moreover, an extensive work on the chain structures with proper characterization is required. In the present work, we attempt at presenting an overall behavior of the fluid chain structure while focusing on the Physics of flow for the primary link by analyzing the dimensional characteristics and velocity field. Special attention is given to the second and third collisions, leading to the formation of the subsequent mutually orthogonal links. In the next section, the numerical framework employed in this work is explained followed by the mesh sensitivity analysis and validation in Section III.

II. NUMERICAL FORMULATION

Collision of liquid jets has been studied using three-dimensional two-phase flow simulations using the finite volume framework for discretization and Volume Of Fluid (VOF) approach for interface tracking. Open source time-dependent, multi-fluid Navier-Stokes solver, Gerris is used for the current study (Popinet, 2003). Gerris has been successful used frequently by researchers, such as Chen *et al.* (2013); Kumar, Das, and Mitra (2016, 2017), to delve into similar problems in interfacial flows involving liquid sheets, jets and thin features like ligaments and films to capture intricate flow details and investigate the process. It invokes an adaptive mesh projection method for solution of incompressible continuity and momentum equations. The spatial discretization of the domain is undertaken using an

octree based structured hierachal grid system, which can be locally refined. Equation 1 contains the mass conservation equation for the incompressible flow, which simply states that the velocity field ($V_i = V_1\hat{i} + V_2\hat{j} + V_3\hat{k}$) must be divergence free.

$$\frac{\partial V_i}{\partial X_i} = 0 \quad (1)$$

The momentum equation for the incompressible Newtonian fluids that is solved for all three spatial coordinates can be summarized as given in equation 2. In the equation, the forces applied on the control volume chosen consist of the pressure in form of its gradient field ($\frac{\partial p}{\partial X_i}$), the volume specific body force due to gravitation (ρg_i), the surface forces due to shear stress ($2\mu D_{ik}$, where μ represents the coefficient of dynamic viscosity and D_{ik} is the deformation tensor) and the interface specific surface tension force ($\sigma\kappa$, where σ is the surface tension coefficient and κ denotes the curvature of interface).

$$\rho \left(\frac{\partial V_i}{\partial t} + V_k \frac{\partial V_i}{\partial X_k} \right) = - \frac{\partial p}{\partial X_i} + \frac{\partial (2\mu D_{ik})}{\partial X_k} + \sigma\kappa\delta_s m_i + \rho g_i \quad (2)$$

Moreover, the surface tension term is multiplied with the Dirac distribution function (δ_s) to ensure that the force by surface tension is concentrated at the interface having the normal vector m_i . Further, the deformation tensor D_{ik} is defined using the symmetric part of the velocity field gradient as given in Equation 3.

$$D_{ik} = \frac{1}{2} \left(\frac{\partial V_i}{\partial X_k} + \frac{\partial V_k}{\partial X_i} \right) \quad (3)$$

The Equation 2 (Navier Stokes) implicitly implies the conservation of the mechanical energy. Moreover, the temperature variations are too small to affect the phenomenon being investigated and therefore, no thermal energy equation is employed. The interface tracking is undertaken using the Volume Of Fluid (VOF) approach. For this, a volume fraction (tracer) is defined as $\Psi(x_i, t)$, at the spatial and temporal instance of x_i and t respectively. Therefore, the density and viscosity for the study can be defined as given by Equation 4. The Volume of Fluid approach implemented is a two-step process of interface reconstruction (based on the values of Ψ and piecewise linear interface construction scheme, PLIC) along with geometric flux computation and interface advection. Equation 5 represents the advection equation for the volume fraction field.

$$A(\Psi) = \Psi A_1 + (1 - \Psi) A_2 \quad \forall A \in \{\rho, \mu\} \quad (4)$$

$$\frac{\partial \Psi}{\partial t} + \frac{\partial(\Psi V_i)}{\partial X_i} = 0 \quad (5)$$

Second order accurate time discretization of momentum and continuity equations are carried out with time splitting algorithm as proposed by Chorin (1968), whereby an unconditionally stable corrector predictor time marching approach is adopted. A multi-grid solver is used for solution of the resulting pressure-velocity coupled Laplace equation. The advection term of the momentum equation $\left(V_k \frac{\partial V_i}{\partial X_k}\right)$ is estimated using the Bell-Colella-Glaz second-order unsplit upwind scheme (Bell, Colella, and Glaz, 1989), which requires the restriction to be set up on the time step between subsequent outer iterations based on the Courant-Friedrichs-Lowy (CFL) stability criteria as the estimation is stable only for $CFL < 1$ (Popinet, 2009). The details of the octree-based multi-level solver employed for the solution of the system of the equations can be found in the works of Popinet (2003, 2009).

Figure 1 illustrates the computational domain with dimensions $40d_j \times 10d_j \times 10d_j$. The lateral surfaces are kept at a distance of $5d_j$ to avoid any biasing from the boundaries. These surfaces along with the bottom one are kept as standard boundary outflow. Two small liquid jets inclined at an angle of α from the vertical are initialized at the start of the simulation. The boundary condition on the top surface of the computational domain is that of liquid jet inlets, for which a parabolic velocity profile $\left(\left[2 \left(1 - \left(\frac{2r}{d_j} \right)^2 \right) \right] u_j \right)$ is patched, where r is the radial location in the jet from its centerline, d_j is the diameter of the liquid jets and u_j is the average inlet velocity of the jet as illustrated in Figure 1. We restrict ourselves in the laminar flow regime where the formation of stable liquid chains or sheet structures with closed rim is prominent. Following the Equations 1 to 5 and the boundary conditions, one can easily see that different features of these liquid sheets can be represented in terms of the kinematic and dynamic properties, such as jet velocity (u_j), its diameter (d_j), angle of impingement (2α), acceleration due to gravity (g) and other physical properties, such as density of the fluid (ρ), its viscosity (μ) and the coefficient of surface tension at the fluid-air interface. On dimensional analysis, different independent PI - terms are recognized as given in Equation 6. On the left hand side we have different chain and link features, such as the length of individual lengths of the link, its maximum extent in the the plane of the formation of the liquid sheet, the average fluid velocity in the liquid sheet $\left(\frac{u_0}{u_j} = \int_0^1 \int_0^1 \int_0^1 \frac{\sqrt{V_i V_i}}{u_j} d\left(\frac{Y}{h}\right) d\left(\frac{r}{r_{max}}\right) d\left(\frac{\theta}{2\pi}\right) \right)$ and the thickness of the liquid sheet at different spatial locations $\left(\frac{h}{d_j} \right)$. Further, on the right hand side of the equation, different

non-dimensional numbers can be recognized based on flow and geometric properties. The first term can be identified as the Froude number ($Fr = \frac{u_j}{\sqrt{gd_j}}$), which acts as a measure of the relative strength of the inertia of the liquid jet and the force of gravity. Gravity is taken in the positive x-direction as shown in Figure 1. Second term is the Bond number ($Bo = \frac{\rho gd_j^2}{\sigma}$), used to account for the strength of the surface tension force as compared with the gravity body force on the chain structure. The viscosity comes into consideration with the term given by ($\frac{\mu}{\rho\sqrt{gd_j^3}}$), which can be simplified as the ratio between the Reynolds number ($Re = \frac{\rho u_j d_j}{\mu}$) and the Froude number of the jet (Fr).

$$\left(\frac{l_i}{d_j}, \frac{d_i}{d_j}, \frac{u_0}{u_j}, \frac{h}{d_j} \right) = \Pi \left(\frac{u_j}{\sqrt{gd_j}}, \frac{\rho gd_j^2}{\sigma}, \frac{\mu}{\rho\sqrt{gd_j^3}}, \alpha \right) \quad (6)$$

With the development of the above Mathematical model, it is necessary to check for mesh sensitivity to the solution and further validation with the experimental results present in the literature, which has been carried out in the next section.

III. MESH SENSITIVITY ANALYSIS AND MODEL VALIDATION

Sensitivity to the mesh refinement is analyzed in this section along with validation of the numerical results. Gerris uses an adaptive octree mode of refinement as illustrated in Figure 2. It is necessary to capture the smallest features of the flow, in this case, the thickness of the liquid sheet. The multi-level grid structure adapts itself according to the gradient of the tracer Ψ , which implies that the structured octree mesh is finest at the interface between the two fluids. Hasson and Peck (1964) gave a simple expression to quantify the thickness of the liquid sheet which takes the form of Equation 7. This expression has been found to describe the thickness of liquid sheet within experimental precision by several independent researchers (Shen and Poulikakos, 1998; Choo and Kang, 2001; Ekimova *et al.*, 2015).

$$\frac{hr}{d_j^2} = \frac{1}{4} \frac{\sin^3 \alpha}{(1 - \cos \theta \cos \alpha)^2} \quad (7)$$

Although the minimum of Equation 7 occurs at $\theta \rightarrow \pi$, it must be noted that the decrement in thickness is more because of the increase in radial distance downstream of the first collision point ($h \propto \frac{1}{r}$), which is maximum near low azimuthal angles (Figures 2b(iv) and 1b, just upstream of the second collision point). This happens because the fluid velocity increases

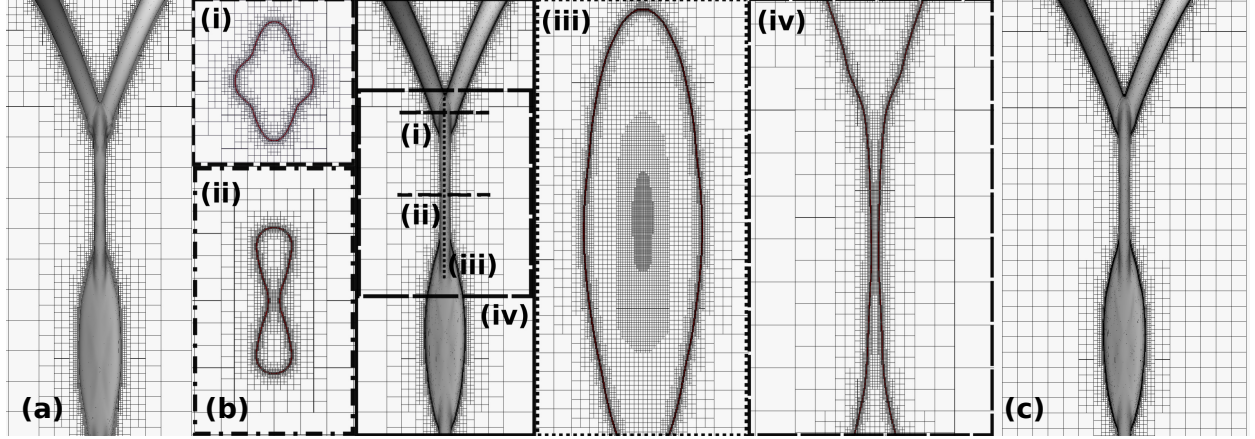


FIG. 2. Representation of the Adaptive Mesh Refinement (AMR) technique used by Gerris, the grid is finest at the interface of the two phases. Flow parameters used for Grid Independence Study (GIS) are $\alpha = 30^\circ$, $Fr = 2$, $Bo = 3.4$ and $Re/Fr = 1100$, with $d_j/\delta l =$ (a) 51.2,(b) 102.4 and (c) 204.8. Sub-figures in (b) show mesh refinement at different sections of the structure (i) YZ plane at the point of collision of the jets, (ii) XZ plane of the midsection of the primary link, (iii) XZ plane view of the primary link and (iv) XY plane view of the primary link, where the minimum thickness can be clearly identified immediately upstream of the second collision.

as the gravitational potential is converted to kinetic energy and the thickness decreases to keep the mass flow rate constant. An order of magnitude analysis reveals that $\frac{hr}{d_j^2} \sim 1$ for the minimum thickness at $2\alpha = \frac{\pi}{2}$ in the range of our numerical simulations. Therefore, $\frac{d_j}{\delta l} \sim 10 \frac{r_{max}}{d_j}$ can be used as an imperative starting point for the grid independence study. The factor of 10 is included to have at least 10 grid points across the smallest length scale for the structure to be fully resolved (Ling, Zaleski, and Scardovelli, 2015), else the sheet thickness will be equal to the minimum grid size and the sheet would break at the cost of being unresolved (Chen *et al.*, 2013). Figure 3 gives a representative case employed for the grid independence study. Applying above discussed arguments, $\frac{d_j}{\delta l} \sim 70$ (Figure 2a) should be ideal for the simulations. It can be clearly seen that the variations in the results such as the contour of the tracer (volume fraction) and velocity profiles at different locations downstream of the collision point, saturate if the refinement is increased from $\frac{d_j}{\delta l} = 102.4$ (Figure 2b) to 204.8 (Figure 2c). Moreover, the later requires more computational power and time (Table I). Therefore, a refinement level of $\frac{d_j}{\delta l} = 102.4$ is employed for this case. A similar analysis is carried out for all the cases reported in the present study initiated with

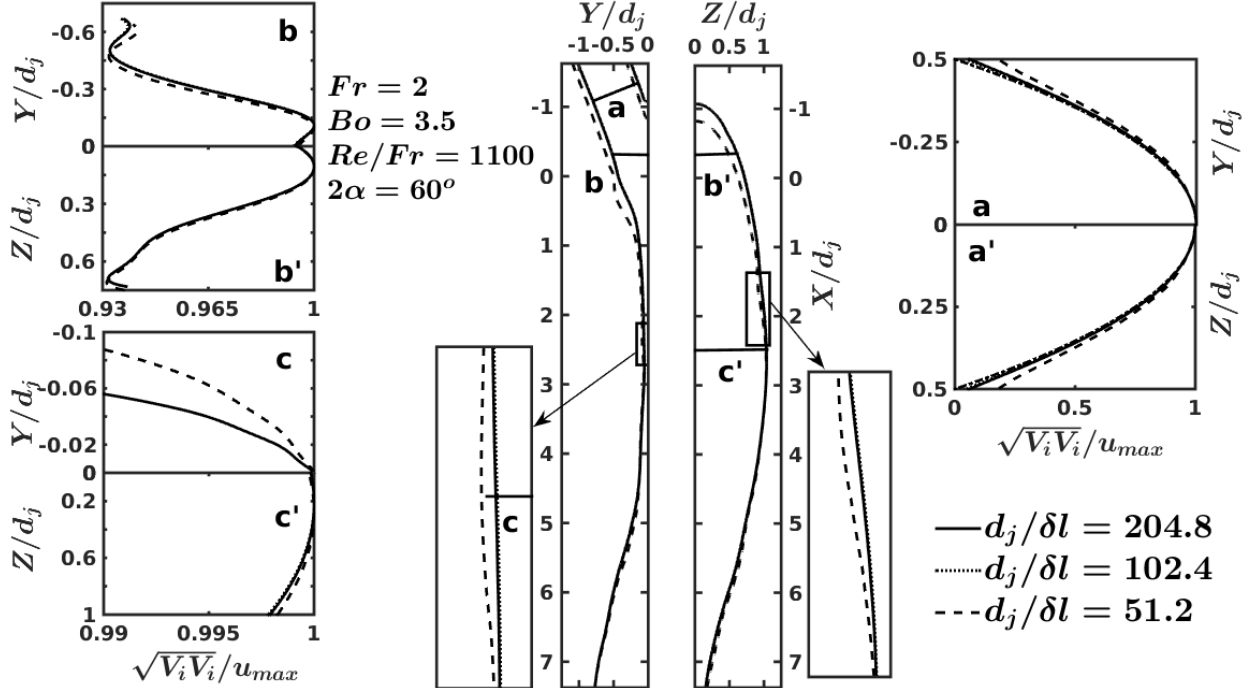


FIG. 3. Illustration of the results of Mesh Sensitivity Analysis for a typical chain structure, having $\alpha = 30^\circ$, $Fr = 2$, $Bo = 3.4$ and $Re/Fr = 1100$. The volume fraction (Ψ) contours (main figures and magnified in inset) show saturation on increasing the refinement from $d_j/\delta l = 102.4$ to 204.8. Velocity profiles at different sections across the chain structure are shown for (a-a') Inside the liquid jet, (b-b') Just downstream of the point of collision and (c-c') At the plane of maximum extent of the liquid sheet.

$\frac{d_j}{\delta l} = 10 \frac{r_{max}}{d_j}$, with $r_{max} = 10d_j$. If the sheet is still not fully resolved or the maximum radial extent of a given link goes higher than $10d_j$, the refinement level is increased.

Next, we use the experimental results obtained by Bush and Hasha (2004) to validate the employed numerical model. Figure 4 presents a description of the results of this test. The primary link of the chain structure formed is illustrated in Figure 4a, with matching between the experimentally obtained boundary of the link and the contour generated from numerical simulations shown in Figure 4b. Making use of the fact that their experiments led to a supercritical (greater than the capillary wave speed) sheet speeds, Bush and Hasha (2004) were able to construct the variation of the liquid volume flux ($Q(\theta) = \frac{dQ}{d\theta} = uhr$) inside the sheet by scanning across the sheet and collecting liquid through a fine opening. Figure 4c shows the variation of the liquid flux with the azimuthal angle inside the sheet along with

TABLE I. Performance data of the processors used for simulations to determine the refinement level in the Grid Independence Study. The simulations are done using four Intel Core i7-6500U CPU having clock speed of 2.5GHz each and 8 GB RAM.

| $\left(\frac{d_j}{\delta l}\right)_{max}$ | $\left(\frac{t_{CPU}}{t_{actual}}\right)$ (days/s) |
|---|---|
| 51.2 | ~ 20 |
| 102.4 | ~ 28 |
| 204.8 | ~ 60 |

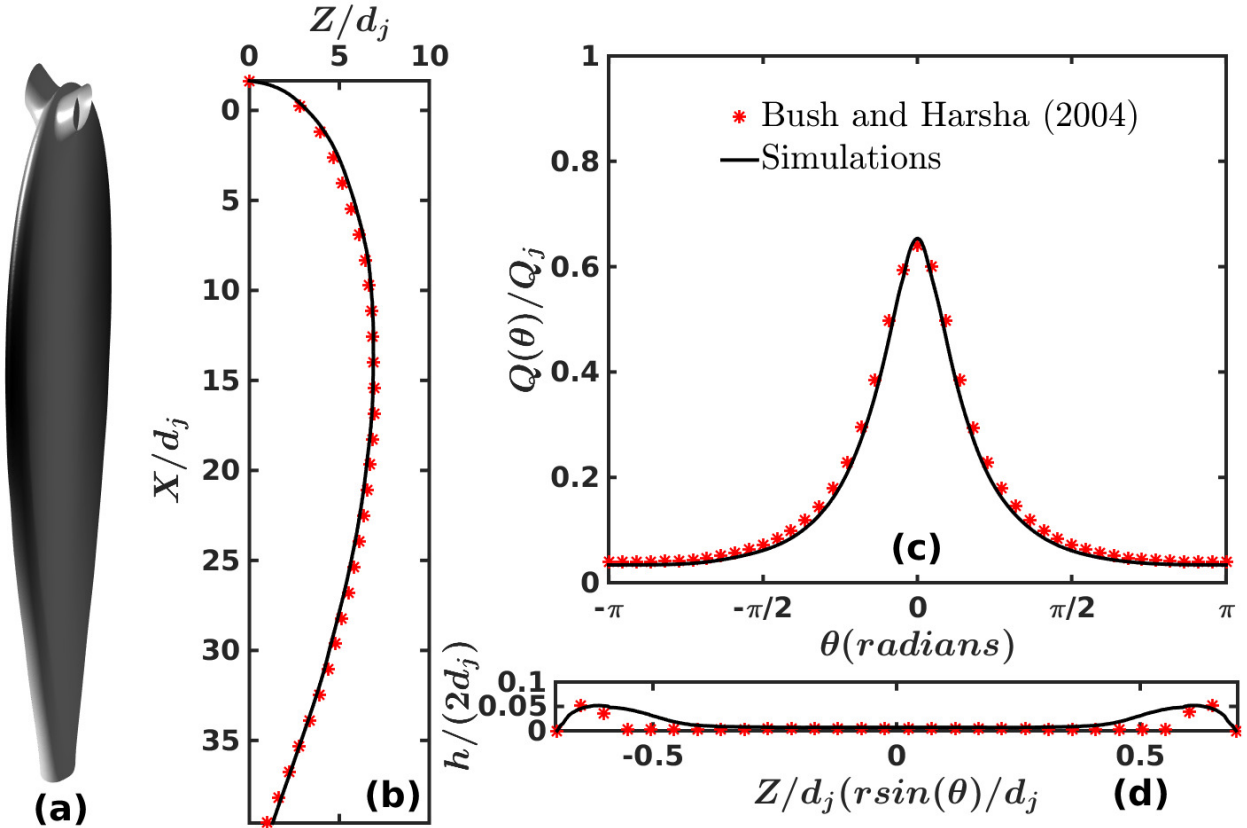


FIG. 4. Validation of the numerical model employed with the experimental results obtained by Bush and Hasha (2004): (a) The iso-surface volume fraction contour showing the primary link of the chain, (b) Volume fraction contour in the X-Z plane at $y = 0$ showing the boundary of the primary link, (c) Variation of the liquid volume flux ($Q(\theta)$), non-dimensionalized with the volume flow rate of the jet, Q_j) and (d) Thickness profile of the liquid sheet obtained at a distance of $17.25d_j$ from the point of the first collision.

the reconstruction of the flux profile by our numerical simulation. Moreover, the thickness of the liquid sheet is one of the major attributes that must be predicted by the numerical simulations. Figure 4d gives a one-to-one correspondence between the thickness profile obtained at a distance of $17.25d_j$ from the point of the first collision. One can clearly observe the presence of a thick rim at the periphery of the sheet. Next, the transient process of impact of the liquid jets is analyzed, followed by the kinematic description of the flow inside the sheet using the velocity profile analysis and an outlook of the streamlines.

IV. COLLISION AND SHEET FORMATION

As the laminar liquid jets collide, a thin liquid sheet bounded by thicker rim is formed in the median plane, perpendicular to the axes of the jets. In this section, the initial transient process of liquid jet collision is discussed. Figure 5 contains the different stages of this process. The initialization of the liquid jets is done using a small inclined cylinder with circular cross-section, across which a parabolic velocity profile is patched as discussed in Section II. These symmetric jets pre-collision are shown in Figure 5a. The reference for temporal variations is kept at the instant when the two jets collide (Figure 1b). The fluid parcels are dispatched radially outwards from the point of impingement. In case of head on collision of liquid jets ($\alpha = 90$), the sheet formed is always radial in absence of gravity (Eggers and Villermaux, 2008) and the point of stagnation is in-line with the two liquid jets which collide (Inamura and Shirota, 2014). However, in this case a bias in the direction of the flow of jets can be observed immediately after the collision as the sheet grows in the direction of gravity and jet inertia (Figure 5c). It must be noted that role of gravity was neglected by Bush and Hasha (2004); Bremond and Villermaux (2006) as the Froude numbers (Fr) in their experiments were high (~ 50) but it plays a crucial role in the analysis with $Fr \sim 1 - 10$.

With further growth of the sheet, a thick bounding rim starts to develop as observed in Figure 5d. This happens because of the accumulation of the fluid parcels at the periphery. In absence of surface tension or at very high Weber number flows, this sheet will keep on expanding, leading to formation of the open rim structures Taylor (1960); Chen *et al.* (2013). In the present study with comparable strength of inertia and surface tension, the structure tries to go towards the state of minimum surface energy and therefore the primary

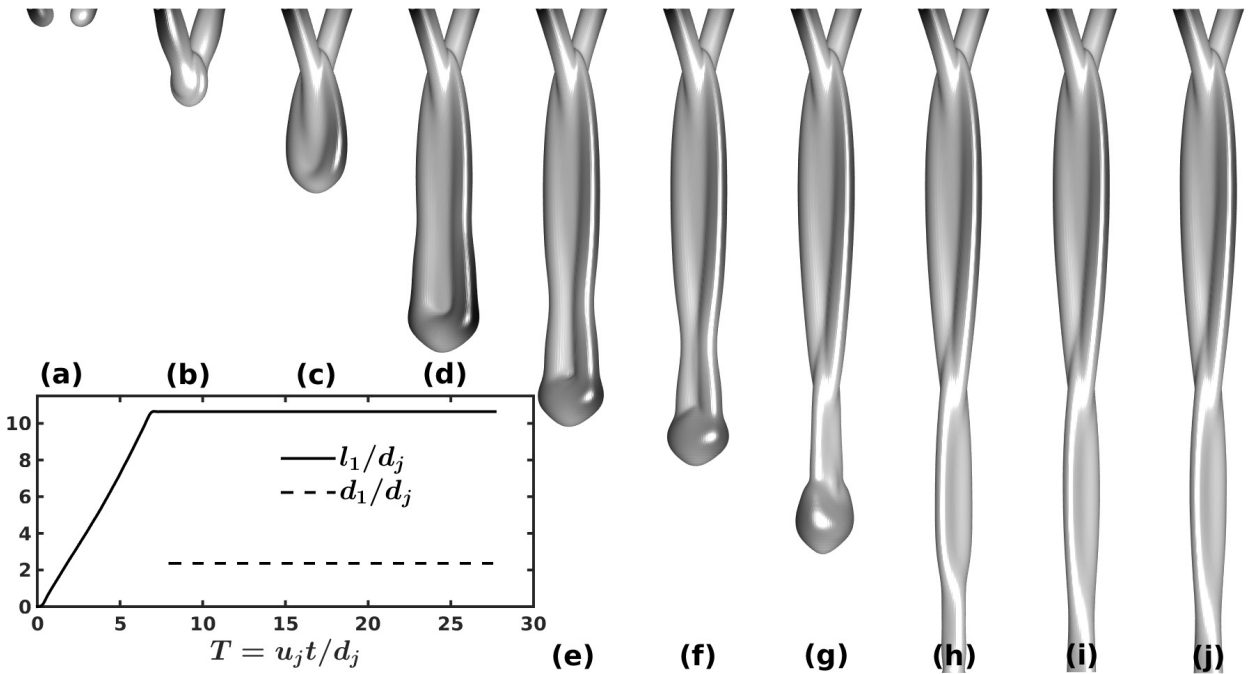


FIG. 5. Transition to the steady state fluid-links chain formed by collision of laminar jets. The figure illustrates the transient period through the temporal advancement from (a) pre-collision symmetric jets to $T(\frac{u_j t}{d_j}) =$ (b) 1.5, (c) 4, (d) 5, (e) 5.5, (f) 6.5, (g) 8.5, (h) 16.5, (i) and (j) 20

link closes as shown in Figure 5e. Surface tension not only puts a check on the expansion of the sheet but also provides the necessary centripetal acceleration to the fluid parcels in the rim, a fact that has been exploited in development of the analytical model for this process. As the sheet closes onto itself, the two rims at the periphery undergo an oblique collision (Figure 5f) at an angle smaller than the initial collision. Post secondary impingement, similar to Figure 5c, a flow biased sheet begins to develop (Figure 5g). Formation of this secondary link has no affect on the characteristics features of the primary link as the sheet speed is supercritical, and therefore can be independently studied. Temporal advancement results in formation of a full-fledged secondary link as shown in Figure 5h. It must be noted that the plane of formation of this sheet is orthogonal to that of the primary link and therefore the secondary link shares the same plane as the axes of the jets. The process continues and a series of mutually orthogonal links are obtained, successively reducing in size until, a long single liquid jet is formed (Bush and Hasha, 2004). The state of the chain structure for the primary link can be taken as to pertain towards a steady state after $T(\frac{u_j t}{d_j}) = 8.5$ (Figure 5g) with no visible changes from Figure 5h to 5j. As long as the flow configuration

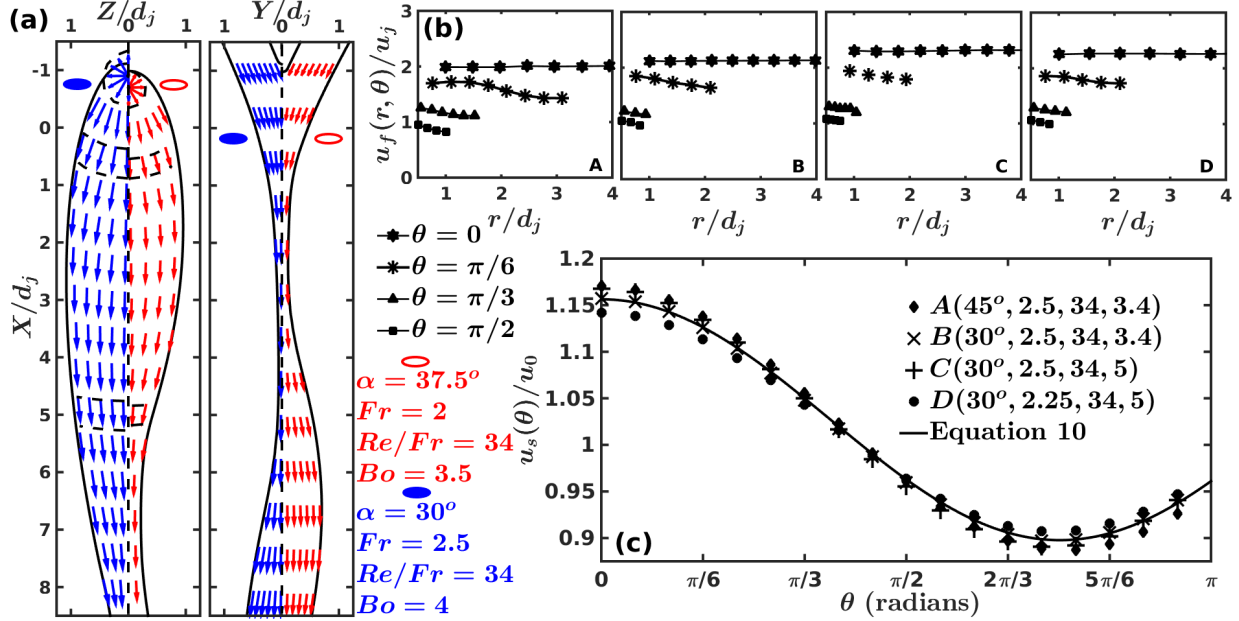


FIG. 6. Flow kinematics of the fluid parcels inside the liquid sheet: (a) Velocity vector field for two representative cases with different flow and physical parameters, the vector field is radial near the stagnation point and then follows the self similar phase contour, (b) Variation of velocity in the radial direction for four representative cases with $(\alpha, Fr, Re/Fr, Bo)$: A($45^\circ, 2.5, 34, 3.4$), B($30^\circ, 2.5, 34, 3.4$), C($30^\circ, 2.5, 34, 5$) and D($30^\circ, 2.25, 34, 5$) and (c) Variation of the radially averaged sheet velocity (u_s), non-dimensionalized with the average sheet velocity (u_0) along the azimuthal direction in the sheet.

is suited for this regime, the chain structure is stable and can be used to analyze the various aspects of the interaction of liquid jets to form a sheet. Next, a description based on the flow kinematics is discussed for chain structures.

V. KINEMATICS OF THE FLOW

In case of the collision of symmetric liquid jets, the net component of velocities in the plane perpendicular to the median sheet plane ($u_j \sin \alpha$) vanishes to conserve momentum and contributes only to the radial spread of the sheet and not the bias in direction of gravity. If the collision is head on, the velocity vectors emerge radially from the point of collision which is also the stagnation point. However, in case of oblique collision, the stagnation point shifts upstream to the point where the two axes meet on the median plane (Choo and

Kang, 2007; Yang *et al.*, 2014) and has been found by Inamura and Shirota (2014) (given as $\delta s = \lambda d_j / (2 \sin \alpha)$, where the factor λ is a function of the impingement angle) using the continuity and momentum equations. The effect can be clearly observed in the velocity vector fields illustrated in Figure 6a, where the velocity vectors seem to be emerging from a stagnation point upstream of the point of impact. Further on moving downstream, the vectors follows self-similar paths as traced by the sheet boundary. These velocity vectors are constructed using the average flow across the thickness of the sheet at a given radial and azimuthal point in space ($u_f(r, \theta)$, given by Equation 8).

$$u_f(r, \theta) = \int_0^1 \sqrt{V_i V_i} d(Y/h) \quad (8)$$

The variation of this fluid velocity ($u_f(r, \theta)$) with the radial direction is illustrated in Figure 6b for four different cases with varying flow and physical parameters. It can be observed that the order of change in the fluid velocity across the radial distance from the point of impact is less than the change across the azimuthal direction. This was first reported by Choo and Kang (2002) for obtuse angle impingements ($2\alpha \gtrsim 90^\circ$). Therefore, the sheet velocity (u_s) can be found by solving the integral in Equation 9. In most of the numerical analysis, this quantity has been taken as constant and equal to the jet velocity at the time of impact (Bush and Hasha, 2004; Bremond and Villermaux, 2006; Hasson and Peck, 1964). However, the sheet velocity is actually a function of the azimuthal angle and flow parameters.

$$u_s = \int_0^1 u_f(r, \theta) d(r/r_{max}) \quad (9)$$

Once, the sheet velocity is non dimensionalized with the overall average sheet velocity ($u_0 = \int_0^1 u_s d(\theta/(2\pi))$), self similar velocity profile is obtained as shown in Figure 6c and is given by Equation 10.

$$\frac{u_s(\theta)}{u_0} = 1.03 + 0.13 \cos \left(\frac{4.18\theta}{\pi} \right) \quad (10)$$

It must be noted that the average sheet velocity u_0 is a function of different flow and physical parameters and can be represented in terms of non-dimensional quantities, as given in Equation 6. Once the average sheet velocity exceeds a critical value, the chain structure is no longer stable as the Kelvin - Helmholtz instability kicks in (Villermaux and Clanet, 2002). The discussion so far only gives an idea about the two-dimensional velocity field responsible for the shape and size of the links. Next we discuss the three dimensional velocity field with an aid of streamlines and vectors at different locations to explain the subsequent collisions

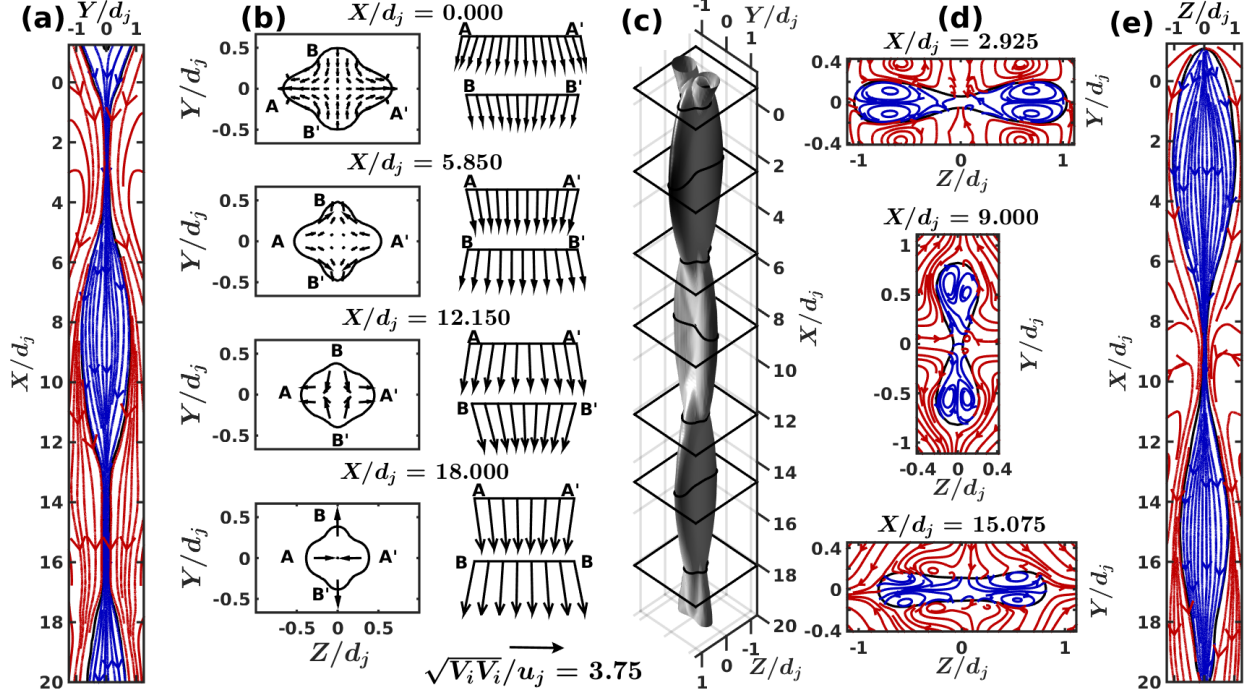


FIG. 7. Details of the three dimensional velocity field, (a) Streamlines in the XY plane, that is the plane of the axes of liquid jets: red streamlines are for the air velocity field and blue for the liquid, (b) Velocity vector field as viewed in the YZ plane at different collision locations in the chain structure showing the converging (jet or rim impact) and diverging (formation of liquid sheet) tendencies, (c) The three dimensional stable chain structure formed for $\alpha = 30^\circ$, $Fr = 2$, $Re/Fr = 1125$ and $Bo = 3.4$, (d) Streamlines in the YZ plane at the locations of maximum width in respective links of the chain and (e) Streamlines in the plane of the primary and tertiary links (here XZ).

which gives rise to the chain structure in Figure 7. The streamlines in both liquid and air media follows steadily the phase contour boundary, with the streamlines inside the chain structure going in trajectories similar to the outer boundary as shown in Figures 7a and 7e. These coherent structure gives stability to the flow sustaining it in space and time. The shift in stagnation point upstream of the point of impact discussed in previous paragraphs acts as the point of initiation of the streamlines in the XZ plane (Figure 7e). The primary link is formed by collision of liquid jets at the origin whereas the subsequent links are formed by collision of the thick rims of the preceding links. Figure 7b illustrates these collision planes. At $X/d_j = 0$, the liquid jets converge onto themselves (B-B') marked by retracting

velocity field, whereas the liquid sheet grows (A-A') in Z direction, marked by an expanding velocity field. Similar trends are observed at all collision planes ($X/d_j = 5.85, 12.15$ and 18) leading to the formation of four visible links in this case (Figure 7c). The velocity vector magnitudes goes on increasing at each subsequent collision planes as the gravitational head is converted to dynamic head leading to narrowing of the extend of liquid phase boundary in the XZ plane. In the primary link, this converging-diverging trend is continued from above the first collision point to the plane where extent of the link perpendicular to the net flow direction in the plane of the link is maximum. As illustrated in Figure 7d, the streamlines at the location of maximum width imply that the component of velocity perpendicular to the liquid sheet phase boundary is zero ($\frac{d\Psi}{dn} = 0$). This results in formation of distinguished circulation patterns both inside and outside the lobes at the locations of maximum extent corresponding to the three links visible in this case.

Observing the three dimensional streamlines in Figure 8, a characteristic twist can be found as the flow propagates downstream through the locations of subsequent collisions that lead to formation of secondary and tertiary links. The twist occurs as the fluid parcels are restricted by surface tension to follow the chain outer periphery. This twist is characterized by the offset of these streamlines from the two mutually orthogonal axes: the XY plane containing the axes of the liquid jets (δz) and the XZ median plane orthogonal to this one (δy). The offset of the most extreme streamline are shown in the inset of Figure 8 for two representative cases having different ratios of Reynolds Number and Froude Number (Re/Fr). The offset of all the streamlines from the XZ plane (δy) decreases continuously as the liquid jets approach each other (retracting velocity field shown in Figure 7b). After collision, a streamline present going towards the median plane is selected. It is observed that δy decreases continuously through the first link, but a transformation is observed at the location of the second collision when the offset tends to increase, reaching the maxima at the location of maximum width of the secondary link. Opposite trend is observed for the XY plane whereby the offset (δz) increases after the first collision continuously till the maximum width of the primary link and then decreases for the secondary link. These variations in the offset in streamlines show the presence of twist every-time it crosses the location of impact, until viscous effects take charge and only a single jet of liquid is left at the end of chain structure. These viscous forces lead to dissipation of energy as the liquids jets (or rims for post primary link) collide with each other. As it would be discussed in Section VI, increasing

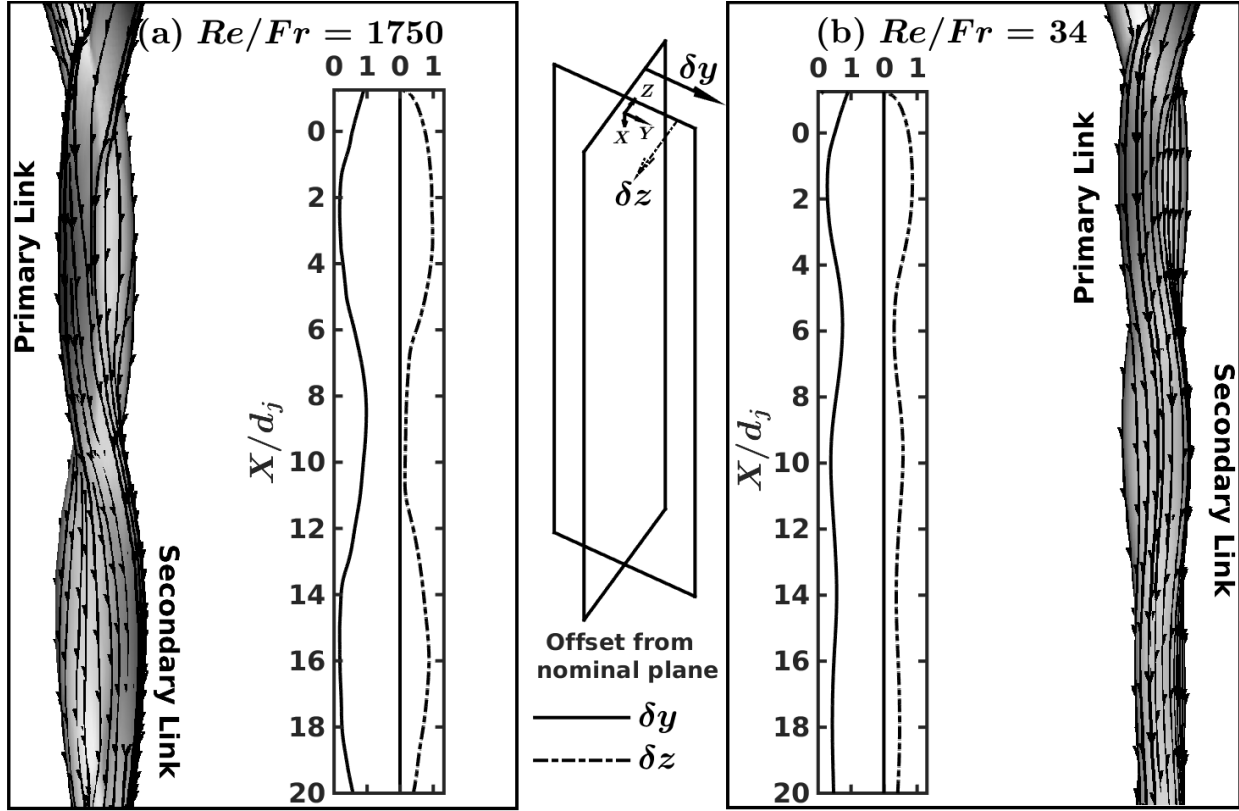


FIG. 8. Three dimensional streamlines embedded on the chain structure illustrating the twist incurred as they traverse through the region of subsequent collisions for $\alpha = 30^\circ$, $Fr = 2$, $Bo = 3.4$ and (a) $Re/Fr = 1750$ and (b) $Re/Fr = 34$. The figures in inset show the offset (δy from XZ plane and δz from XY plane) of the streamline at the extreme end of the chain structure as it moves downstream with the flow for the corresponding cases.

viscosity (decreasing Re/Fr) lead to decrease in the length and width of the links because of an increase in dissipation. Since, the average sheet velocity decreases as well, the thickness for lower Re/Fr is more than its other counterpart (Yang *et al.*, 2014). Therefore, the offset from the median plane perpendicular to the two jets (δy) increases with decreasing Re/Fr because of increased thickness. Moreover, the streamline in case of lower Re/Fr moves towards a constant offset from both the planes relatively earlier than the case with higher Re/Fr because of enhanced action of viscous dissipation for higher viscosities. It is clear from our discussions above, in Section II and in works of Yang *et al.* (2014) that different flow parameters such as the impingement angle (α) and jet inertia (characterized by jet velocity u_j and diameter d_j) along with properties like viscosity and surface tension

TABLE II. Variations of different parameters affecting the chain structure

| α | Fr | Re/Fr | Bo |
|----------|------|---------|-----------|
| 10°-45° | 0.5 | -4 | 12.5-2000 |

play a crucial role in the determination of the three dimensional stable chain structures and therefore, the next section is devoted to analyze such effects.

VI. EFFECTS OF PROPERTY VARIATIONS ON CHAIN STRUCTURE

Yang *et al.* (2014) acknowledged the importance of parametric variations on collision process and their results for the effects of these parameters on the first link of the chain (Figure 9) can be easily generalized for the entire chain structure (Figure 10). Ranges of different non-dimensional parameters introduced in Section II used in our numerical simulations are given in Table II. In the previous sections, we realized that subsequent links of the chain structure are formed due to impact of the rims in preceding links. These collision processes result in the dissipation of energy similar to the case of inelastic collisions of billiards balls which is deformation and friction dominant (Irodov, 1980). The collision of these cylindrical jets and rims is inertia and viscous forces dominant. Keeping all other parameters constant, decreasing the viscosity (increasing Re/Fr) leads to considerable increase in sheet dimensions at low Re/Fr but the effect is reduced substantially at higher Re/Fr as shown in Figure 10a (change in Re/Fr from 12.5 to 187.5 as compared to increase from 187.5 to 1725). It can be explained by the fact at higher viscosities (low Re/Fr , Figure 9d) lead to severe dissipation and diminishing of links, but after a certain level the effect of viscosity is overshadowed by the interplay between inertia and surface tension and there is not much change in shape and size of links. It can also be noticed that it is the viscous dissipations that result in decrement in the size of subsequent links leading to a point where the sheet loses its identity, giving rise to a single jet of fluid. The effect is prominent in Figure 10a for $Re/Fr = 12.5$. Moreover, as the jet momentum is increased by increasing the Fr , the resulting links that are formed are bigger in size (Figure 9b) as the fluid inertia is a direct measure of the expansion tendency of the link. One can clearly see that this effect is transmitted to the subsequent links as well.

Further, surface tension is an important entity which keeps a check on the expansion ten-

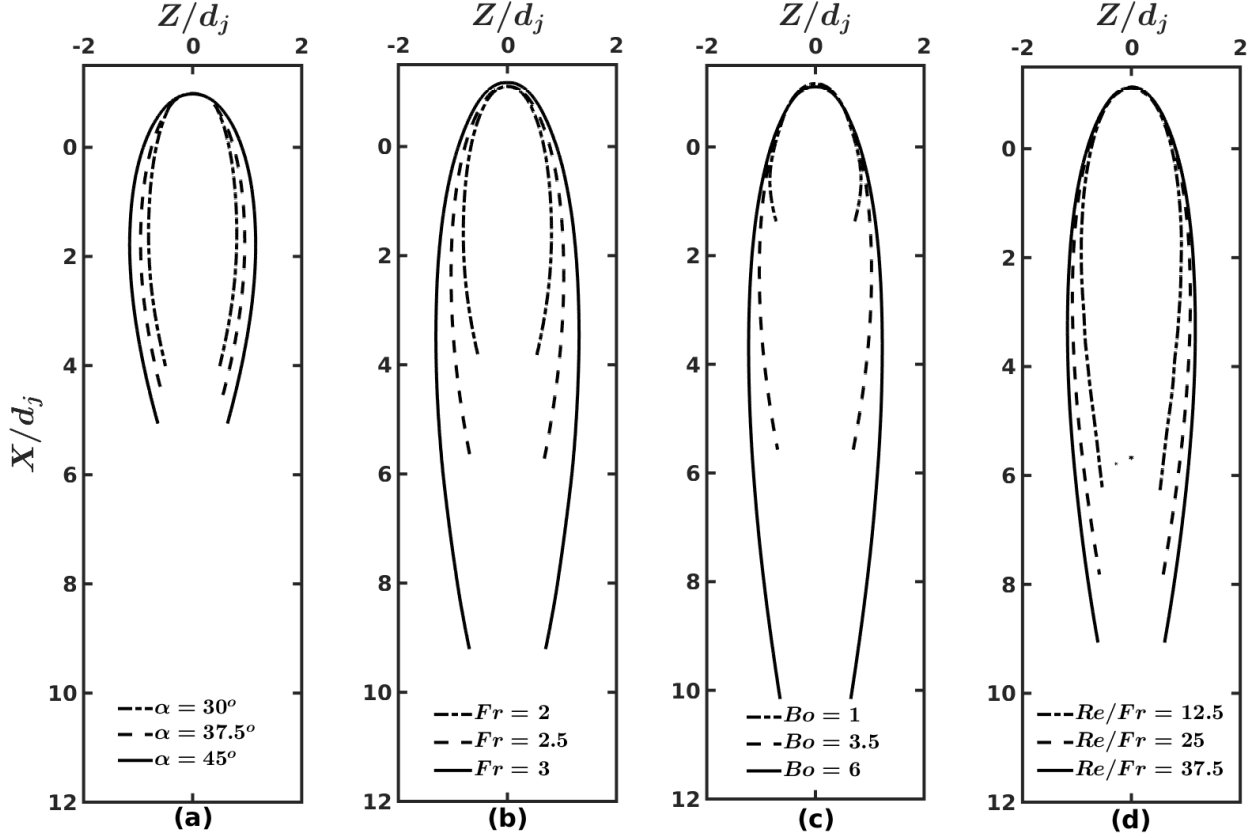


FIG. 9. Change in parameter affecting the characteristics of the first link formed by the collision of laminar liquid jets for variation in (a) Impingement angle α at $Fr = 2.5$, $Re/Fr = 34$ and $Bo = 4.57$, (b) Froude number Fr at $\alpha = 30^\circ$, $Re/Fr = 34$ and $Bo = 3.4$, (c) Bond number Bo at $\alpha = 30^\circ$, $Fr = 2.5$ and $Re/Fr = 34$ and (d) Ratio of Reynolds number and Froude number Re/Fr at $\alpha = 30^\circ$, $Fr = 2$ and $Bo = 3.4$

dencies of the link. It also provides the necessary centripetal acceleration to the fluid parcels in the rim. As the surface tension is decreased (Bond number Bo increased), the link can expand further and stops when the surface tension force balances the inertial centrifugal force giving a significantly bigger link for larger Bo as seen in Figures 9c and 10c. If the surface tension force is not enough to maintain equilibrium (on further increasing of the jet inertia), the rim becomes unstable and finger like protrusions can be observed leading to the formation of droplets resulting from Plateau-Rayleigh instability (Bremond and Villermaux, 2006). As the surface tension is increased keeping all other parameters constant (low Bo regime), the system tries to go towards the minimum surface energy decreasing the dimensions of the corresponding links (primary link in Figure 9 from $Bo = 6$ to 1). Unlike the

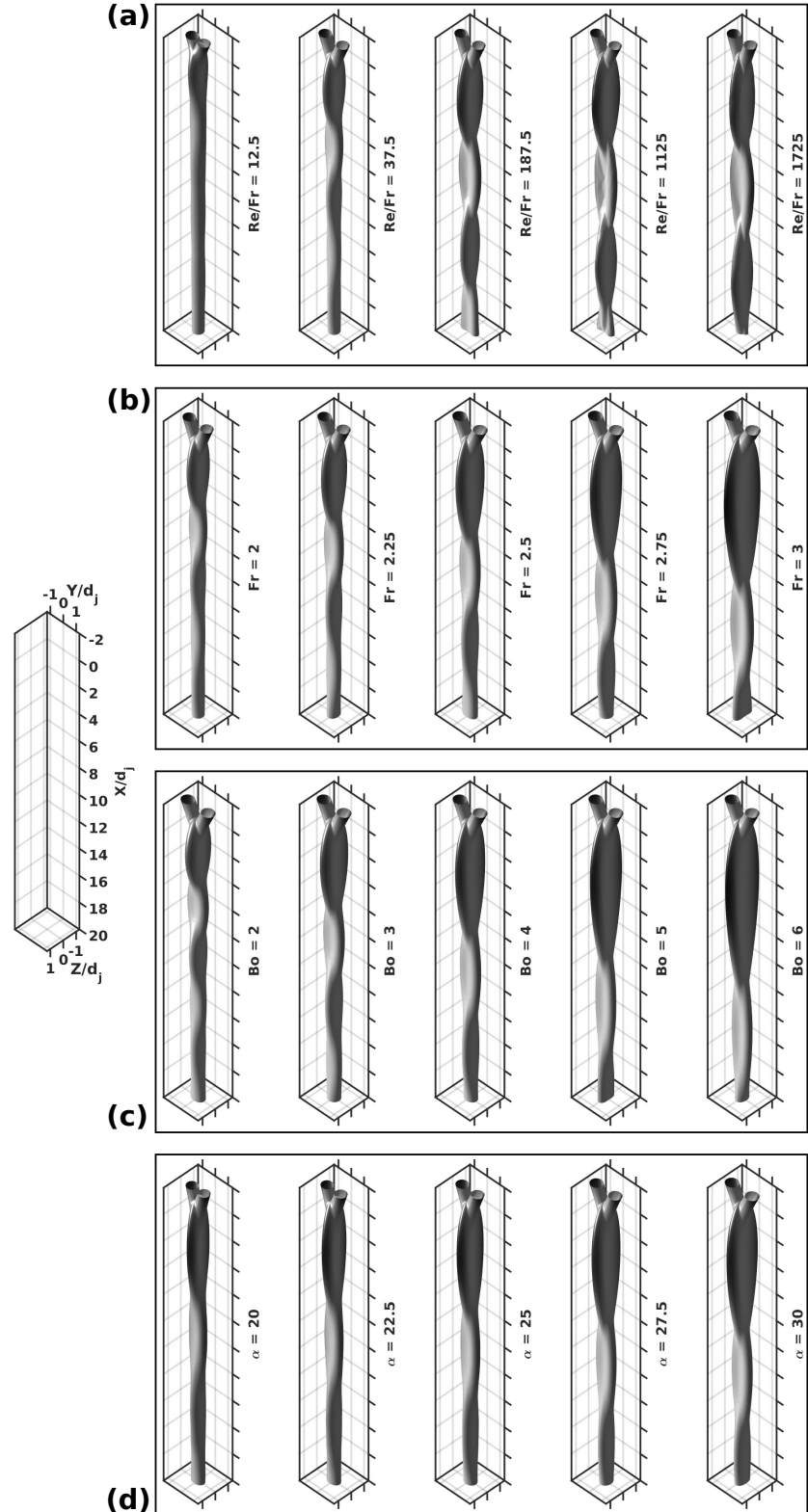


FIG. 10. High fidelity numerical simulations of liquid jets collision to form chain structure for variation of (a) Re/Fr at $Fr = 2, Bo = 3.4, \alpha = 30$ (b) Fr at $Re/Fr = 34, Bo = 3.4, \alpha = 30$ (c) Bo at $Re/Fr = 34, Fr = 2.5, \alpha = 30$ and (d) α at $Re/Fr = 34, Fr = 2.5, Bo = 4.57$

low Reynolds number regime, distinct and comparable secondary as well as tertiary links are visible (Figure 10c, $Bo = 2$). Finally, as the impingement angle is increased, the jet momentum in direction of gravity decreases (because of decrease in $u_j \cos \alpha$). However, the component of jet momentum perpendicular to the median plane increases leading to plump looking liquid sheets (substantial increase in width at same order of length) as shown in Figures 9a and 10d. This follows logically from the fact that in case of head-on liquid jet collisions ($2\alpha = 180^\circ$), the only bias in the sheet is created by the action of gravity, resulting in a limiting case radial sheet. Using the information obtained from the wide range of parametric variations, in the next section, models to predict the shape and size of individual links are formulated.

VII. PREDICTING THE SHAPE OF AN INDIVIDUAL LINK

Prediction of shape and size of the individual links is really important for chain structure and there have been several attempts for the same Bush and Hasha (2004); Bremond and Villermaux (2006). However, in most of the cases, it is required to take input from the experiments to close the system of equations as the link characteristics are not just a spatial functions but the coefficients involved are also dependent on flow, geometric and physical parameters. The need to close differential equations developed can be overcome by full scale numerical simulations in three dimensions, but it would be handy if we have an in-line equation to describe the shape and size of the first link. Next, we discuss two such models, the correlation model is formed by regression analysis and the billiards balls analogy model has been formulated using different forces that act on the fluid parcel as it traverses along the periphery of the sheet.

A. Co-relation model

Numerical simulations are done over the range of parameters given in Table II. At a given abscissa X , the distance between the two extremities of the fluid sheet in the plane of the sheet is given by $\Delta Z(x)$. Utilizing the fact that the sheet is symmetric about the $Z = 0$ plane, a third order polynomial fit is used to get the spatial variation of the non-dimensional sheet extent ($\Delta Z/(2d_j)$) as a function of the non-dimensional downstream abscissa coordinate

TABLE III. Factors ($C_{m,n}$) involved in Equation 12 determined by regression analysis to get the coefficients p_n of Equation 11

| | C_0 | C_1 | C_2 | C_3 | C_4 |
|-------|-------|--------|--------|--------|--------|
| p_0 | 3.662 | -0.082 | -2.822 | -1.504 | -0.657 |
| p_1 | 2.720 | 0.490 | -1.231 | -0.831 | -0.290 |
| p_2 | 0.353 | 1.146 | 0.437 | 0.074 | 0.029 |
| p_3 | 0.512 | 0.592 | 0.800 | -0.065 | 0.039 |

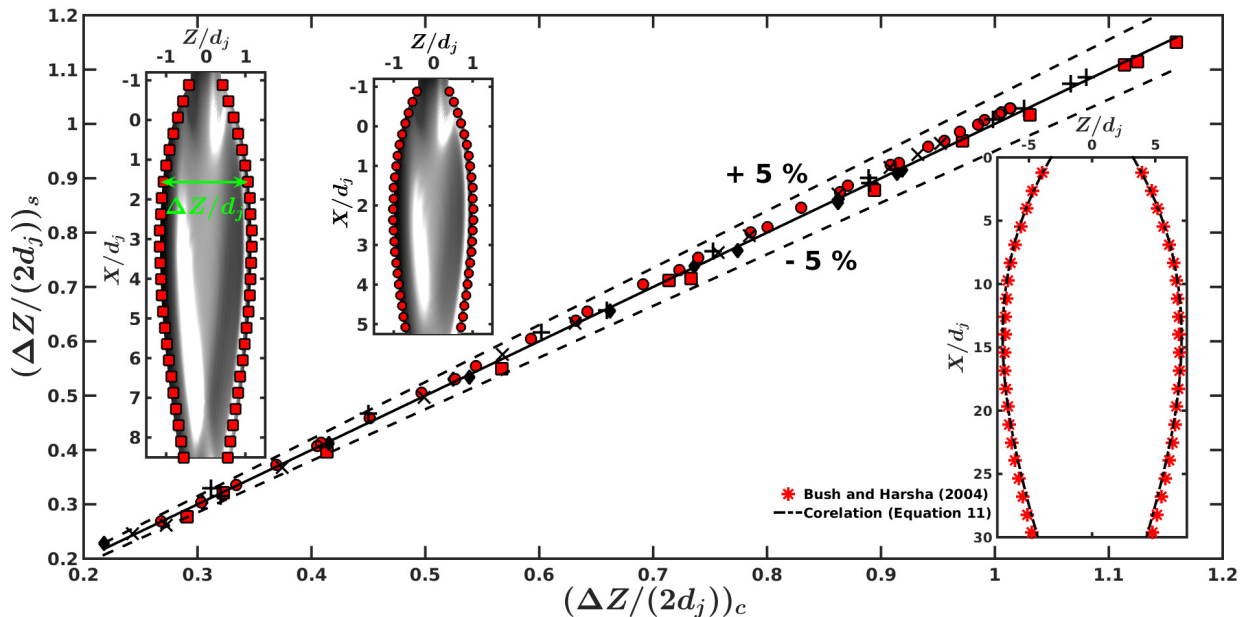


FIG. 11. Comparison between the values of expansion of the sheet outer periphery ($\Delta Z(x)$) as obtained from correlations ($(\Delta Z/(2d_j))_c$) given in Equation 11 and from numerical simulations ($(\Delta Z/(2d_j))_s$) for different parametric variations of testing data with (symbol, α , Fr , Re/Fr , Bo) = (\blacksquare , 30° , 2.5, 34, 5); first inset figure from the left; (+, 30° , 2.5, 34, 4); (\blacklozenge , 30° , 2.5, 20, 2.3); (\times , 25° , 2.5, 34, 4.57) and (\bullet , 30° , 2.5, 20, 3.75); second inset figure from the left. In the last inset figure (from the left), comparison between the correlation model given in Equation 11 and experimental results of Bush and Hasha (2004) is provided.

(X/d_j) , as given in Equation 11. The goodness of fit parameter, R squared norm (R^2) has been ensured to never go below 0.975 and sum of squared error (SSE) never exceeds 0.01.

$$\frac{\Delta Z}{2d_j} = \sum_{n=0}^{n=3} p_n \left(\frac{X}{d_j} \right)^n \quad (11)$$

Once the coefficients (p_n) are found for Equation 11, it is necessary to relate them with the different non-dimensional control parameters given in Equation 6. Therefore, power law factors are formed through linear regression analysis to yield these coefficients as described by Equation 12. Respective factors ($C_{m,n}$) are provided in Table 12. The R squared goodness of regression norm in this case never goes below 0.925 for any of the four regression analysis involved.

$$p_n = C_{0,n} (\sin \alpha)^{C_{1,n}} (Fr)^{C_{2,n}} (Bo)^{C_{3,n}} (Re/Fr)^{C_{4,n}} \quad (12)$$

The discussed correlation model is then tested with five test cases with different flow parameters and configurations selected at random which were not a part of the either of the polynomial fitting or the regression analysis done to complete Equation 11. The predicted $((\Delta Z)/(2d_j))_c$ values and those obtained from simulations $((\Delta Z)/(2d_j))_s$ are then compared in Figure 11. It can be observed that the scatter plot points, all lie in the narrow band of $\pm 5\%$ error region and therefore the Equations 11 and 12 can be used satisfactorily to get the extent of an individual link for any flow configuration in the chain regime of liquid jets collision. Next, we present an analytical model to predict the shape and size of an individual link in order to get insight into the Physics of the phenomenon.

B. Analytical model

Since the time of Newton, point objects like billiards balls have been used to analyze the effect of different forces on the system. When the two liquid jets collide, the fluid parcels are all thrown radially outwards. If we consider only the plane of the liquid sheet, the process can be assumed to be same as collision of two billiard balls. Based on the coefficient of restitution (e) of the impact, the balls can follow one of many self-similar trajectories. In absence of any forces, the balls follow a linear path post collision with impact having $e = 0$ following the median plane and the others traveling through linear paths forming a triangular region, which transforms to parabolic trajectories in presence of gravity along the direction perpendicular to the relative velocity of the balls. This results in formation of expanding trajectories which would happen in absence of surface tension with the liquid sheets as well (Taylor, 1960). Therefore, to mimic the effect of surface tension, a constant magnitude force f_n is applied, which is always perpendicular to the velocity of individual balls post collision. The free body diagram and schematic of the proposed model is illustrated in Figure 12c.

Point of collision is chosen as the origin. The initial boundary conditions, immediately after collision are summarized in Equation 13, where $\zeta(X)$ is trajectory of the ball, v_{ball} is the velocity of the ball and ϕ_0 is the initial angle of ejection of the billiard ball.

$$\text{At } X = 0 \begin{cases} \zeta = 0 \\ v_{ball,0} = v_i \sqrt{\cos^2 \alpha + e^2 \sin^2 \alpha} \\ \phi_0 = \tan^{-1}(e \tan \alpha) \end{cases} \quad (13)$$

In the direction tangential to the trajectory of the ball (along the velocity of ball), a component of body force, gravity ($mg \cos \alpha$) provides the necessary acceleration, $a_t = v_{ball} \frac{dv_{ball}}{ds}$ (where s is the distance of the ball from the origin along the trajectory), as given by Equation 14a. Making use of the fact that for small increments $ds \cos \phi = dx$, Equation 14a can be integrated directly to get Equation 14b after inserting the velocity boundary condition from Equation 13. It must be noted that since the force f_n is always perpendicular to the ball, its only effect is to change the direction of motion and has no effect on the magnitude of ball's velocity.

$$v_{ball} \frac{dv_{ball}}{ds} = g \cos \phi \quad (14a)$$

$$v_{ball}^2 = v_{ball,0}^2 + 2gX \quad (14b)$$

In the direction perpendicular to the trajectory of ball, a component of gravity $mg \sin \phi$ and the normal force f_n provides the necessary centripetal acceleration $\frac{v_{ball}^2}{r_c}$ to keep the ball in a curvilinear trajectory, where $r_c(X)$ is the radius of curvature of the trajectory. The force balance is summarized in Equation 15a. These forces keep a track of the effects of surface tension and body forces that provide a check on the expansion of the liquid sheet. Substituting the results obtained from Equation 14a and rearranging, Equation 15b is formulated. Here, Λ contributes to the effects of normal force f_n and is given by $\frac{f_n}{mg}$. Moreover, χ is the inertial length scale, given by $\frac{v_{ball}^2}{2g}$.

$$mg \sin \phi + f_n = m \frac{v_{ball}^2}{r_c} \quad (15a)$$

$$r_c (\sin \phi + \Lambda) = 2\chi \left(\frac{X}{\chi} + 1 \right) \quad (15b)$$

The radius of curvature of the trajectory $\zeta(X)$ is given by the conventional Equation 16.

$$r_c = \left| \frac{\left(1 + \left(\frac{d\zeta}{dX} \right)^2 \right)^{3/2}}{\frac{d^2\zeta}{dX^2}} \right| \quad (16)$$

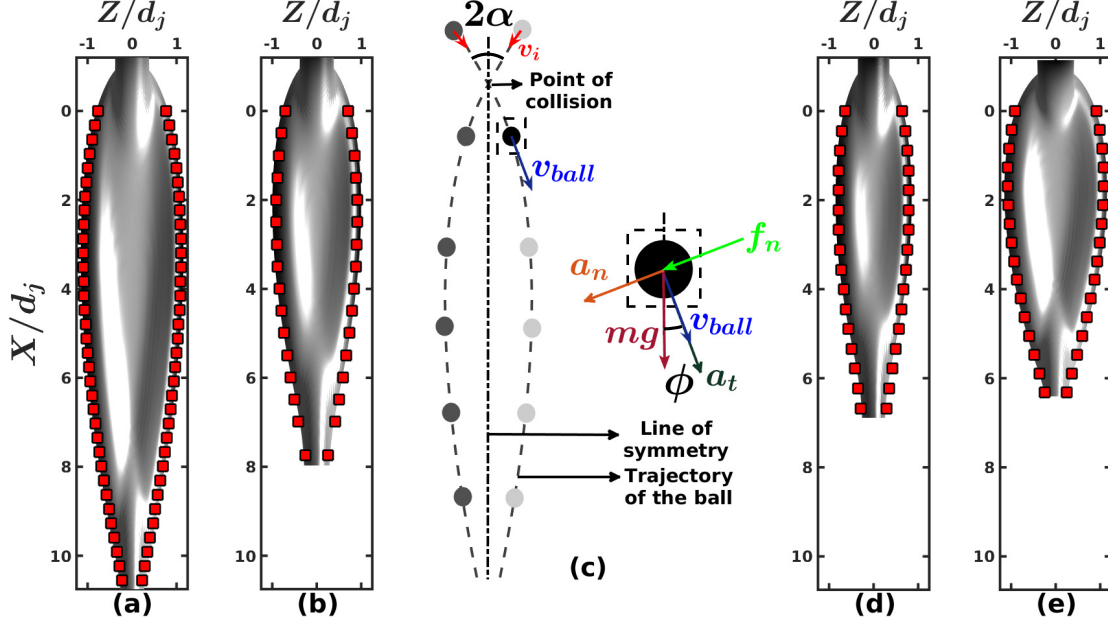


FIG. 12. Comparison between the link shape and dimension obtained through numerical simulations (iso-surface volume contours) and by using the analytical model using force balance (red colored symbols ■) for different flow configurations ($\alpha, Fr, Re/Fr, Bo, \epsilon$): (a) (), (b) (), (d) () and (e) (), where ϵ is the L^1 relative error norm given by Equation 19. In Figure (c), the schematic of this analytical model is shown.

Implementing the geometric relations like $\frac{d\zeta}{dX} = \tan \phi$ into the expression for the radius of curvature r_c , the Equation 15b can be modified to get the Equation 17a, which can further be integrated to get Equation 17b using the boundary condition on the initial angle of ejection ϕ_0 given in Equation 13.

$$2\chi \cos \phi \frac{d\phi}{dX} = \frac{\sin \phi + \Lambda}{\left(\frac{X}{\chi} + 1\right)} \quad (17a)$$

$$\sin \phi - \sin \phi_0 = (\Lambda + \sin \phi_0) \left(\frac{1}{\sqrt{\frac{X}{\chi} + 1}} - 1 \right) \quad (17b)$$

Recalling that $\tan \phi = \frac{d\zeta}{dX}$, the above equation can be finally converted to Equation 18, where the parameter $\eta \sin \phi = \Lambda$ needs to be evaluated for every case, which is done based on the seek and find algorithm. The domain for η is kept as all positive real numbers (that is $\eta \in \mathbb{R}^+$). At the limiting case $\eta \rightarrow 0$, the system behaves as if only gravity is acting on the balls and the corresponding sheet would be always open and expanding. As a measure

of the precision of the seek and find algorithm, the L^1 error norm, ϵ is selected, which is given by Equation 19, where $(X_m, \zeta_a(X_m))$ is the location of the ball found by integrating Equation 18 and $(X_m, \zeta_s(X_m))$ is the location of the outer periphery of the liquid sheet. The instance of η for which ϵ is minimum is selected. The maximum value of ϵ tolerated for the simulations with parameters mentioned in Table II is 10%.

$$\frac{d\zeta}{dX} = \tan \left\{ \sin^{-1} \left[\sin \phi_0 (1 + \eta) \left(\frac{1}{\sqrt{\frac{X}{x}} + 1} - 1 \right) \right] \right\} \quad (18)$$

$$\epsilon = \frac{1}{N} \sum_{m=1}^N \left| \frac{\zeta_a(X_m) - \zeta_s(X_m)}{\zeta_s(X_m)} \right| \quad (19)$$

Once η is found for all the simulation points explored in the present study, a linear regression analysis is carried out to get the power law factors as given in Equation 20. The R squared goodness of regression norm for this is kept above 0.99.

$$\eta = 3.28 (\sin \alpha)^{-0.077} (Fr)^{0.418} (Bo)^{-0.248} (Re/Fr)^{-0.084} \quad (20)$$

Figure 12 illustrates the comparison of the numerical simulation with the analytical model proposed. For this four different parametric cases are selected which did not participate in the method elaborated above and are found to adhere to the ϵ values of less than 5%. With this analytical model, we demonstrate the effects of several forces on the system of two jets collision leading to the formation of the primary link. Next, we focus on the formation of secondary and tertiary links resulting from the collision of rims of primary and secondary links respectively.

VIII. COLLISIONS TO FORM SUBSEQUENT LINKS

IX. CONCLUSIONS

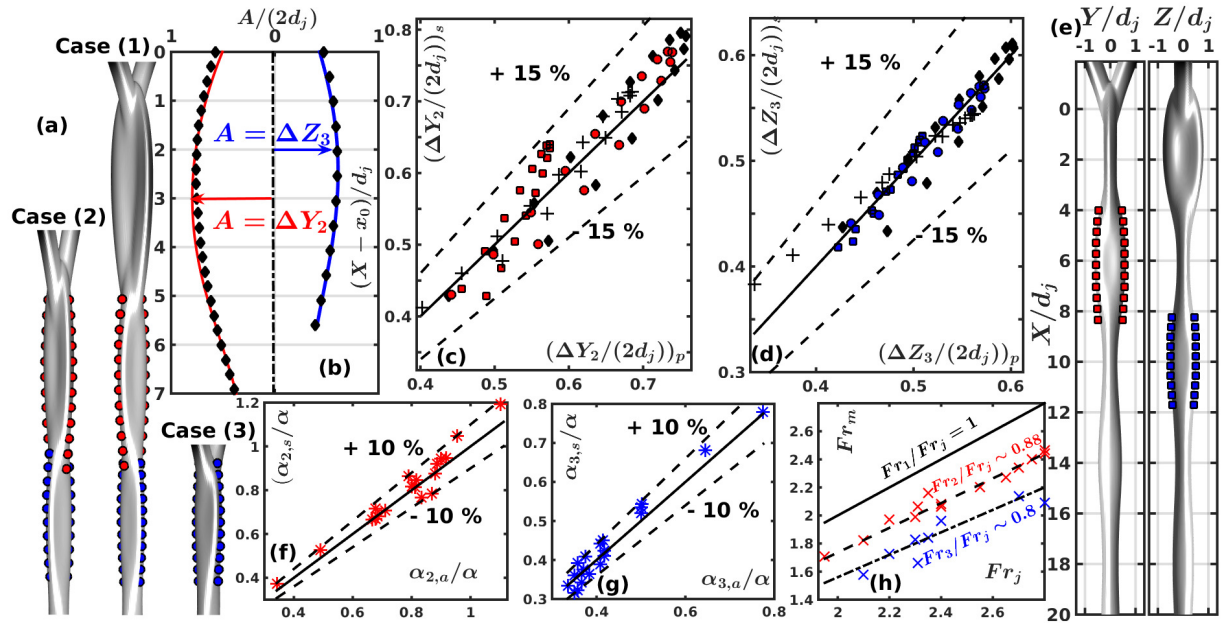


FIG. 13.

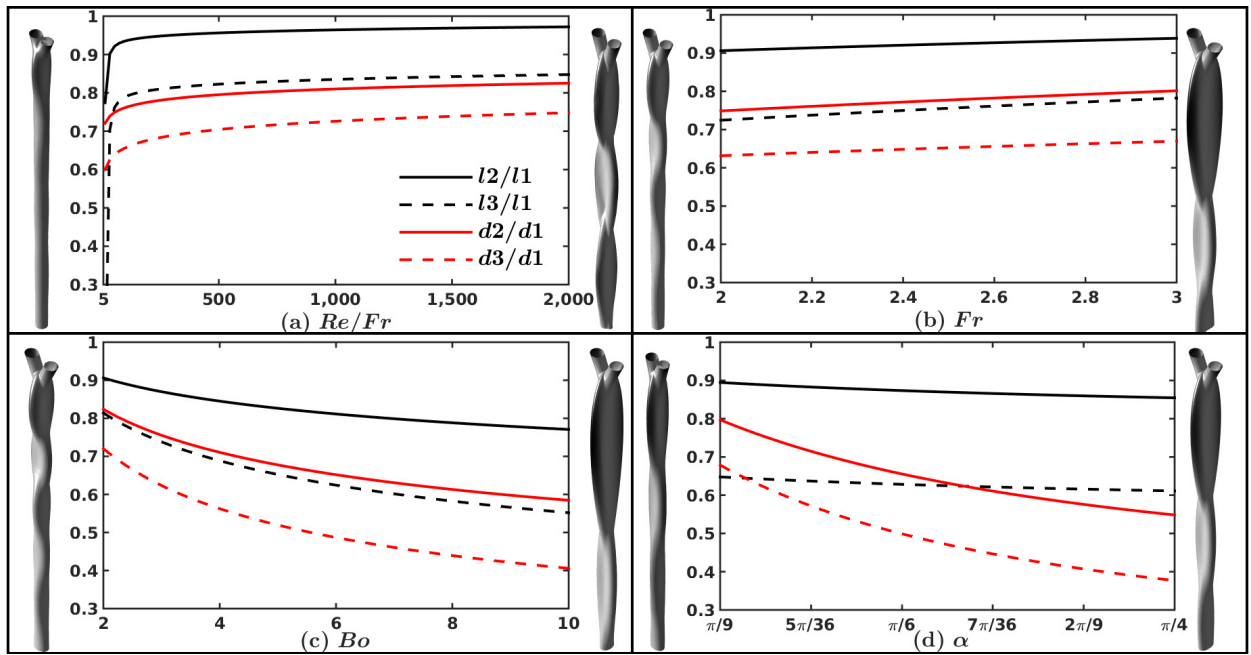


FIG. 14.

REFERENCES

- Arienti, M., Li, X., Soteriou, M. C., Eckett, C. A., Sussman, M., and Jensen, R., “Coupled level-set/volume-of-fluid method for simulation of injector atomization,” *Journal of Propulsion and Power* **29**, 147–157 (2012).
- Bell, J. B., Colella, P., and Glaz, H. M., “A second-order projection method for the incompressible navier-stokes equations,” *Journal of Computational Physics* **85**, 257–283 (1989).
- Bremond, N. and Villermaux, E., “Atomization by jet impact,” *Journal of Fluid Mechanics* **549**, 273–306 (2006).
- Bush, J. W. and Hasha, A. E., “On the collision of laminar jets: fluid chains and fishbones,” *Journal of fluid mechanics* **511**, 285–310 (2004).
- Chen, X., Ma, D., Yang, V., and Popinet, S., “High-fidelity simulations of impinging jet atomization,” *Atomization and Sprays* **23** (2013).
- Choo, Y. and Kang, B., “Parametric study on impinging-jet liquid sheet thickness distribution using an interferometric method,” *Experiments in fluids* **31**, 56–62 (2001).
- Choo, Y. and Kang, B., “The effect of jet velocity profile on the characteristics of thickness and velocity of the liquid sheet formed by two impinging jets,” *Physics of Fluids* **19**, 112101 (2007).
- Choo, Y.-J. and Kang, B.-S., “The velocity distribution of the liquid sheet formed by two low-speed impinging jets,” *Physics of fluids* **14**, 622–627 (2002).
- Chorin, A. J., “Numerical solution of the navier-stokes equations,” *Mathematics of computation* **22**, 745–762 (1968).
- Da, F., Hahn, D., Batty, C., Wojtan, C., and Grinspun, E., “Surface-only liquids,” *ACM Transactions on Graphics (TOG)* **35**, 78 (2016).
- Da Vinci, L., Schneider, M., and Gingerich, O., *Der Codex Leicester* (Richter, 1999).
- Dombrowski, N. and Fraser, R., “A photographic investigation into the disintegration of liquid sheets,” *Philosophical Transactions of the Royal Society of London. Series A, Mathematical and Physical Sciences* , 101–130 (1954).
- Eggers, J. and Villermaux, E., “Physics of liquid jets,” *Reports on progress in physics* **71**, 036601 (2008).
- Ekimova, M., Quevedo, W., Faubel, M., Wernet, P., and Nibbering, E. T., “A liquid flatjet system for solution phase soft-x-ray spectroscopy,” *Structural Dynamics* **2**, 054301 (2015).

- Erni, P. and Elabbadi, A., “Free impinging jet microreactors: controlling reactive flows via surface tension and fluid viscoelasticity,” *Langmuir* **29**, 7812–7824 (2013).
- Hasson, D. and Peck, R. E., “Thickness distribution in a sheet formed by impinging jets,” *AIChE Journal* **10**, 752–754 (1964).
- Hureau, J. and Weber, R., “Impinging free jets of ideal fluid,” *Journal of Fluid Mechanics* **372**, 357–374 (1998).
- Ibrahim, E. and Przekwas, A., “Impinging jets atomization,” *Physics of Fluids A: Fluid Dynamics* **3**, 2981–2987 (1991).
- Inamura, T. and Shirota, M., “Effect of velocity profile of impinging jets on sheet characteristics formed by impingement of two round liquid jets,” *International Journal of Multiphase Flow* **60**, 149–160 (2014).
- Inoue, C., Watanabe, T., and Himeno, T., “Study on atomization process of liquid sheet formed by impinging jets,” in *44th AIAA/ASME/SAE/ASEE Joint Propulsion Conference & Exhibit* (2008) p. 4847.
- Inoue, C., Watanabe, T., and Himeno, T., “Liquid sheet dynamics and primary breakup characteristics at impingement type injector,” in *45th AIAA/ASME/SAE/ASEE Joint Propulsion Conference & Exhibit* (2009) p. 5041.
- Irodov, I. E., *Fundamental laws of mechanics* (Mir, 1980).
- Kumar, P., Das, A. K., and Mitra, S. K., “Physical understanding of gas-liquid annular flow and its transition to dispersed droplets,” *Physics of Fluids* **28**, 072101 (2016).
- Kumar, P., Das, A. K., and Mitra, S. K., “Bending and growth of entrained air filament under converging and asymmetric rotational fields,” *Physics of Fluids* **29**, 022101 (2017).
- Lhuissier, H. and Villermaux, E., “The destabilization of an initially thick liquid sheet edge,” *Physics of Fluids* **23**, 091705 (2011).
- Ling, Y., Zaleski, S., and Scardovelli, R., “Multiscale simulation of atomization with small droplets represented by a lagrangian point-particle model,” *International Journal of Multiphase Flow* **76**, 122–143 (2015).
- Ma, D.-J., Chen, X.-D., Khare, P., and Yang, V., “Atomization patterns and breakup characteristics of liquid sheets formed by two impinging jets,” in *49th AIAA Aerospace Sciences Meeting including the New Horizons Forum and Aerospace Exposition* (2011) p. 97.

- Miller Jr, K. D., “Distribution of spray from impinging liquid jets,” *Journal of Applied Physics* **31**, 1132–1133 (1960).
- Popinet, S., “Gerris: a tree-based adaptive solver for the incompressible euler equations in complex geometries,” *Journal of Computational Physics* **190**, 572–600 (2003).
- Popinet, S., “An accurate adaptive solver for surface-tension-driven interfacial flows,” *Journal of Computational Physics* **228**, 5838–5866 (2009).
- Rayleigh, L., “On the capillary phenomena of jets,” in *Proc. R. Soc. London*, Vol. 29 (1879) pp. 71–97.
- Shen, Y. B. and Poulikakos, D., “Thickness variation of a liquid sheet formed by two impinging jets using holographic interferometry,” *ASME Journal of Fluids Engineering* **120**, 482–487 (1998).
- Sussman, M., Smith, K. M., Hussaini, M. Y., Ohta, M., and Zhi-Wei, R., “A sharp interface method for incompressible two-phase flows,” *Journal of computational physics* **221**, 469–505 (2007).
- Taylor, G., “Formation of thin flat sheets of water,” in *Proceedings of the Royal Society of London A: Mathematical, Physical and Engineering Sciences*, Vol. 259 (The Royal Society, 1960) pp. 1–17.
- Villermaux, E. and Clanet, C., “Life of a flapping liquid sheet,” *Journal of fluid mechanics* **462**, 341–363 (2002).
- Wadhwa, N., Vlachos, P., and Jung, S., “Noncoalescence in the oblique collision of fluid jets,” *Physical review letters* **110**, 124502 (2013).
- Yang, L.-j., Zhao, F., Fu, Q.-f., and Cui, K.-d., “Liquid sheet formed by impingement of two viscous jets,” *Journal of Propulsion and Power* **30**, 1016–1026 (2014).
- Zheng, G., Nie, W., Feng, S., and Wu, G., “Numerical simulation of the atomization process of a like-doublet impinging rocket injector,” *Procedia Engineering* **99**, 930–938 (2015).